EUROPEAN ORGANIZATION FOR NUCLEAR RESEARCH

Jet-like correlations with respect to K_S^0 and Λ ($\overline{\Lambda}$) in pp and Pb–Pb collisions at $\sqrt{s_{NN}}$ = 5.02 TeV

ALICE Collaboration

Abstract

Two-particle correlations with K_S^0, $\Lambda/\overline{\Lambda}$, and charged hadrons as trigger particles in the transverse momentum range $8 < p_{T,trig} < 16$ GeV/c, and associated charged particles within $1 < p_{T,assoc} < 8$ GeV/c, are studied at midrapidity in pp and central Pb–Pb collisions at a centre-of-mass energy per nucleon–nucleon collision $\sqrt{s_{NN}} = 5.02$ TeV with the ALICE detector at the LHC. After subtracting the contributions of the flow background, the per-trigger yields are extracted on both the near and away sides, and the ratio in Pb–Pb collisions with respect to pp collisions (I_{AA}) is computed. The per-trigger yield in Pb–Pb collisions on the away side is strongly suppressed to the level of $I_{AA} \approx 0.6$ for $p_{T,assoc} > 3$ GeV/c as expected from strong in-medium energy loss, while an enhancement develops at low $p_{T,assoc}$ on both the near and away sides, reaching $I_{AA} \approx 1.8$ and 2.7 respectively. These findings are in good agreement with previous ALICE measurements from two-particle correlations triggered by neutral pions (π^0–h) and charged hadrons (h–h) in Pb–Pb collisions at $\sqrt{s_{NN}} = 2.76$ TeV. Moreover, the correlations with K_S^0 mesons and $\Lambda/\overline{\Lambda}$ baryons as trigger particles are compared to those of inclusive charged hadrons. The results are compared with the predictions of Monte Carlo models.

arXiv:2211.01197v1 [nucl-ex] 2 Nov 2022

1   Introduction

Ultra-relativistic heavy-ion collisions produce the quark–gluon plasma (QGP), a high-temperature and high-energy-density state of strongly-interacting matter, which is characterised by the deconfinement of the colour charges, quarks and gluons [1–4]. One of the most remarkable signatures of QGP formation is "jet quenching", a modification of the parton showers which is induced by the interactions of energetic quarks and gluons with the medium. One of the manifestations of jet quenching is a reduction of the energy and transverse momentum (p_T) of the jet (and of the hadrons emerging from jet fragmentation) due to medium-induced gluon radiation and collisions with medium constituents [5, 6], usually dubbed as parton energy loss. It is generally measured through the suppression of jets and high-p_T hadron production, and the modification of angular correlations of these hadrons in heavy-ion collisions. The suppression is usually quantified via the nuclear modification factor, R_{AA}, which is defined as the ratio of the particle yield in Pb–Pb collisions to that in pp collisions scaled by the average number of binary nucleon–nucleon collisions [7].

Jet quenching was first observed at the Relativistic Heavy Ion Collider (RHIC) in Au–Au collisions at centre-of-mass energies per nucleon–nucleon collision $\sqrt{s_{NN}}$ = 130 and 200 GeV [8, 9], and then at the Large Hadron Collider (LHC) [7, 10]. At LHC energies, jet quenching can be studied through fully reconstructed jets in heavy-ion collisions at high transverse momentum by measurements of inclusive jet R_{AA} [11–14] and dijet imbalance [15–17], as well as through charged hadron R_{AA} [18–25]. At low transverse momentum of less than 10 GeV/c, uncorrelated background fluctuations due to the underlying event dominate, and event-by-event jet reconstruction becomes difficult. Hence, di-hadron correlations provide an alternative way to study jets in this p_T regime.

Jet suppression has been studied by the ALICE Collaboration at the LHC via the two-particle correlation method [26, 27] with neutral and charged hadrons as trigger particles in Pb–Pb collisions at $\sqrt{s_{NN}} = 2.76$ TeV. Both studies indicate a strong suppression of the per-trigger yield at high associated particle transverse momenta $p_{T,assoc}$ of the away-side peak at an azimuthal angle difference $\Delta\varphi = \pi$ in central Pb–Pb collisions compared to those in pp collisions. Moreover, a strong enhancement has been observed at low $p_{T,assoc}$ of the near-side peak at $\Delta\varphi = 0$. The CMS Collaboration has drawn qualitatively similar conclusions [28]. These effects indicate the presence of a high-opacity medium produced in heavy-ion collisions with which the partons interact along their path.

Jet properties are expected to depend strongly on the species (quark/gluon) and the mass of the parton that initiated the jet, due to the difference in their fragmentation pattern. Differences between quark and gluon jets were observed in e^+e^- annihilations at LEP. A fragmenting gluon emits more soft gluons than a fragmenting quark. Therefore, a gluon-initiated jet typically contains more particles and is characterised by a wider jet cone, while a quark jet is more collimated [29–32]. Furthermore, the fragmentation properties of different parton species in the hot-dense medium created in a heavy-ion collision are also expected to be different for quark- and gluon-initiated jets. Because of its larger colour charge, a gluon jet is supposed to lose more energy than a quark jet [33]. The quark and gluon jet fractions are thus expected to be modified in heavy-ion collisions with respect to pp collisions. The relative hadron production rates in quark and gluon jets seem to differ for K_S^0 and Λ, with baryons produced more copiously in gluon jets [32, 34]. Therefore, the angular correlations involving these hadrons may shed some light on jet quenching effects for jets originating from quark and gluon initiated parton showers, whose interaction amplitude with the medium may differ.

In this article, the measurements of two-particle correlations are presented with K_S^0, $\Lambda/\overline{\Lambda}$, and charged hadrons as trigger particles with transverse momentum $8 < p_{T,trig} < 16$ GeV/c, and associated charged particles with $1 < p_{T,assoc} < 8$ GeV/c, studying their angular difference, $\Delta\varphi$, distributions in pp and Pb–Pb collisions at $\sqrt{s_{NN}} = 5.02$ TeV. These measurements extend the previous ALICE studies of in-medium jet energy loss via angular correlations [26, 27, 35–38] by considering lower $p_{T,assoc}$ charged

hadrons ($p_{T,assoc}$ < 3 GeV/c), and by comparing between meson and baryon as trigger particles including strangeness. These measurements have been extensively used to search for remnants of the radiated energy and the medium response to the high-p_T parton, and further explore possible changes to parton fragmentation patterns and hadronisation mechanisms in the transition from the QGP to a hadron gas.

This article further explores jet quenching effects by studying the nuclear modification factor (I_{AA}), which is defined as the ratio of the jet-like yield from nucleus–nucleus (A–A) collisions to the one from pp collisions. It provides information on the interplay between the parton production spectrum and the energy loss in the medium. On the near side, a deviation of I_{AA} from unity can be connected to a change of the fragmentation function, a change of the quark versus gluon jet ratio, and a bias on the parton p_T spectrum. On the away side, the suppression at high $p_{T,assoc}$ (I_{AA} <1) is evidence of parton energy loss, while the enhancement at low $p_{T,assoc}$ (I_{AA} >1) may involve an interplay of various contributions, such as k_T broadening, medium excitation, as well as fragments from radiated gluons [26, 27, 39].

The article is organised as follows: Sec. 2 provides details on the experimental setup, Sec. 3 describes the data analysis, Sec. 4 is devoted to discussing the results, and Sec. 5 contains the summary.

2 Experimental setup

The ALICE experiment is a multi-purpose detector designed to study hot and dense strongly-interacting matter by measuring particles produced in ultra-relativistic heavy-ion collisions at the LHC. A detailed description of the ALICE detector and its performance can be found in [40, 41]. The apparatus consists of a central barrel with several detectors covering the central rapidity region and positioned inside a solenoidal magnet providing a 0.5 T field parallel to the beam direction and a set of detectors placed at forward and backward rapidities. The detectors used for the present analysis are briefly described in this section. In the central barrel, charged particles are reconstructed using the Inner Tracking System (ITS) and the Time Projection Chamber (TPC), which provide full azimuthal coverage for track reconstruction within a pseudorapidity range of $|\eta| < 0.9$. The ITS is designed to provide tracking near the primary vertex, and is thus a key detector for improving the primary vertex resolution and the reconstruction of secondary vertices from weak decays. The ITS is comprised of six cylindrical layers of silicon detectors surrounding the beam pipe, which make use of three different detector technologies. In the four outer layers, Silicon Drift Detectors (SDD) and Silicon Strip Detectors (SSD) are used for tracking and particle identification. The two innermost layers are equipped with Silicon Pixel Detectors (SPD) covering the intervals $|\eta| < 2$ and $|\eta| < 1.4$, respectively. They provide high-resolution space points for the determination of the primary vertex position and of the track parameters in the vicinity of the beam axis. The TPC is the main tracking detector of the ALICE central barrel. It is a large (88 m^3) cylindrical detector filled with gas. The readout planes, located at the two edges of the drift volume, are composed of 18 azimuthal sectors that cover the full azimuth. Each sector contains 159 pad rows arranged radially. In addition, it performs particle identification (PID) via the measurement of the particle specific energy loss (dE/dx) in the detector gas. Additional information for particle identification is provided by the Time Of Flight (TOF) detector via the measurement of the charged-particle flight time from the interaction point to the detector.

The collision centrality is determined with the V0 detector. The V0 system consists of two scintillator arrays located at asymmetric positions at both sides of the interaction point, one in the pseudorapidity range $2.8 < \eta < 5.1$ (V0A) and the other at $-3.7 < \eta < -1.7$ (V0C), each made of four radial rings with each ring divided into eight sections in the azimuthal direction. It provides a signal proportional to the number of charged particles falling in these acceptance regions. The coincidence of signals in the V0A and V0C is also used to define the minimum-bias interaction trigger.

3   Data analysis

The data sample used in this analysis consists of Pb–Pb collisions at $\sqrt{s_{NN}}$ = 5.02 TeV recorded by the ALICE detector in the 2015 and 2018 LHC data-taking campaigns and pp collisions at $\sqrt{s}$ = 5.02 TeV collected in the year of 2017.

Accepted events are required to match a minimum-bias trigger, with a reconstructed vertex whose distance from the nominal interaction point along the beam direction is within 7 cm and 10 cm in Pb–Pb and pp collisions, respectively. These selection criteria were met by approximately 70 million events in the 0–10% centrality interval in Pb–Pb collisions, corresponding to the 10% most central (highest-multiplicity) collisions, and by approximately 1000 million pp collisions.

The contamination from beam-induced background is removed offline by using the timing information in the V0 detectors and taking into account the correlation between tracklets and clusters with the SPD detector, as discussed in detail in [40]. The contamination from in-bunch pile-up events is removed offline excluding events with multiple vertices reconstructed with the SPD.

The centrality estimation in Pb–Pb collisions is based on the sum of the amplitudes from the two V0 detectors which is proportional to the number of charged particles produced in the V0 acceptance.

The analysis consists of three main parts: (i) K$_S^0$, Λ ($\overline{\Lambda}$), and primary charged particle selection; (ii) construction of the correlation function and of the corresponding corrections; (iii) systematic uncertainty estimation.

3.1   K$_S^0$, Λ ($\overline{\Lambda}$) and primary charged particle selection

The analysis procedure begins with the reconstruction of the trigger and associated particles defined in Sec. 1. The identification and reconstruction of K$_S^0$ and Λ ($\overline{\Lambda}$) particles follows the approach used in previous measurements presented in [42–44], via their most probable decay channels [40] and by exploiting their characteristic V^0 decay topologies:

$$K_S^0 \to \pi^- + \pi^+, \quad BR = 69.2\%,$$

$$\Lambda \to \pi^- + p, \quad\quad BR = 63.9\%,$$

$$\overline{\Lambda} \to \pi^+ + \overline{p}, \quad\quad BR = 63.9\%,$$

where BR denotes the branching ratio [45].

Primary charged particles are reconstructed in the pseudorapidity range $|\eta| < 0.8$ by combining the information from the ITS and TPC detectors (see Sec. 2). To maximise the tracking efficiency and improve the specific energy loss (dE/dx) and momentum resolution for primary charged particles, and guarantee an optimal PID quality, tracks reconstructed with both the TPC and the ITS are required to cross at least 70 TPC readout rows out of a maximum of 159. The ratio of the number of crossed pad-rows to the number of findable clusters (that is the number of geometrically possible clusters which can be assigned to a track) is restricted to be greater than 0.8 (see [40] for the details). The goodness-of-fit values χ^2 per cluster ($\chi^2/N_{clusters}$) of the track fit in the TPC must be less than 2.5. Furthermore, in order to suppress the contamination of secondary particles from weak decays and interactions in the detector material, and ensure uniform distributions in the (η, ϕ) plane, additional selections are applied, leading to the sample of so-called "hybrid" tracks. These are composed of two independent samples of tracks selected with different criteria. The first sample consists of tracks with at least one hit in either of the two SPD layers and small distance of closest approach to the primary vertex. To compensate for the acceptance inhomogeneities introduced by the SPD dead areas and recover good momentum resolution, they are combined with a second sample, which is constituted of tracks without any hit in the two SPD layers but constrained to the primary vertex [46, 47]. Another tracking mode that relies on the

combination of the TPC and the ITS detectors, called global tracking, with tighter selection criteria in addition to requirements for clusters in the SPD or the SDD detectors was used for systematic checks in this analysis.

The identification of V^0 candidates is based on the geometrical selections on the decay topology reported in Table 1 and on the particle identification of their decay products via the measured specific energy loss dE/dx in the TPC. Only V^0 candidates that had daughter tracks within 3σ from the expected energy loss for the correct particle species were used, where σ is the TPC dE/dx resolution (for more details see [40]). The pairs of identified tracks are combined into V^0 candidates, and are accepted if their invariant mass m_{V^0} is within $\pm3\sigma$ from the nominal value of the K_S^0, Λ $(\overline{\Lambda})$ mass [45]. Because of the large combinatorial background in Pb–Pb collisions, a number of topological selections had to be more restrictive than those used in the pp analysis. In particular, more stringent selections were applied on the distance of closest approach (DCA) of the decay tracks to the primary vertex (PV) and on the V^0 radius, which is the distance between the point where the V^0 decays (secondary vertex) and the PV.

To suppress the contamination of Λ reconstructed as K_S^0, a selection is applied on the Armenteros-Podolanski plot, taking the form $p_T^{arm} > 0.2|\alpha^{arm}|$, where p_T^{arm} is the transverse component of the daughter track momentum in the V^0 momentum system and α^{arm} is defined as $\alpha^{arm} = (p_{||}^+ - p_{||}^-)/(p_{||}^+ + p_{||}^-)$, where $p_{||}^+$ $(p_{||}^-)$ is the projection of the positively (negatively) charged decay product momentum on the momentum of the V^0 [48, 49]. Additional selections are applied to remove the V^0 decays reconstructed in the TPC, which are produced in pile-up collisions occurring in different bunch crossings within the TPC readout time. These out-of-bunch pileup events are not rejected by the event selection criteria described above. The criterion for this removal is that at least one of the V^0 daughter tracks is reconstructed in both the ITS and the TPC, or has a signal in the Time-Of-Flight detector.

Table 1: The selection criteria for V^0 candidates. The angle θ_{PA} is defined by the V^0 momentum and the line connecting the PV and the V^0 decay point. The proper lifetime mL/p is calculated with m as the expected V^0 mass under the current hypothesis, L is the distance between the primary and secondary vertices, and p is the particle momentum.

K_S^0 **selection criteria**	**Pb–Pb**	**pp**
DCA of daughter to PV (cm)	> 0.1	> 0.06
DCA between daughters (n_σ)	< 0.8	< 1
$\cos(\theta_{PA})$	> 0.97	> 0.97
V^0 radius (cm)	> 5	> 0.5
Proper lifetime mL/p (cm)	< 20	< 20
Λ $(\overline{\Lambda})$ **selection criteria**	**Pb–Pb**	**pp**
DCA of proton to PV (cm)	> 0.1	> 0.06
DCA of pion to PV (cm)	> 0.25	> 0.06
DCA between daughters (n_σ)	< 0.8	< 1
$\cos(\theta_{PA})$	> 0.995	> 0.98
V^0 radius (cm)	> 5	> 0.5
Proper lifetime mL/p (cm)	< 25	< 30

3.2 Correlation function and corresponding corrections

Unidentified charged particles with transverse momentum within $1 < p_{T,assoc} < 8$ GeV/c associated to V^0 (K_S^0, $\Lambda/\overline{\Lambda}$) and charged hadrons with transverse momentum $8 < p_{T,trig} < 16$ GeV/c are studied via two-particle angular correlations where $p_{T,assoc} < p_{T,trig}$. The correlation function is defined as a function of the azimuthal angle difference $\Delta\varphi = \varphi_{trig} - \varphi_{assoc}$ and pseudorapidity difference $\Delta\eta = \eta_{trig} - \eta_{assoc}$

between trigger and associated particles. It is expressed as

$$C(\Delta\varphi, \Delta\eta) = \frac{1}{N_{\text{trig}}} \frac{\mathrm{d}^2 N_{\text{assoc}}}{\mathrm{d}\Delta\varphi \mathrm{d}\Delta\eta}, \tag{1}$$

where N_{trig} is the number of trigger particles and N_{assoc} is the number of associated particles [35, 42, 50]. Each trigger and each associated particle is weighted with a correction factor that accounts for reconstruction efficiency and contamination by secondary particles. These corrections are applied as a function of η and p_{T}. For the evaluation of the charged-particle reconstruction efficiency, pp collisions are simulated with the Monte Carlo (MC) generator PYTHIA8.125 [51] (Monash 2013 tune [52]), while Pb–Pb collisions are simulated using the HIJING event generator [53]. The generated particles are transported through the apparatus, which is modelled in the simulation using the GEANT3 transport code [54].

Pair acceptance corrections are evaluated with a mixed-event technique, where $(\Delta\varphi, \Delta\eta)$ distributions with the trigger and the associated particles originating from different events with similar multiplicity and PV position along the beam axis are constructed. The mixed-event correlation is scaled to unity with a factor equal to the average of $\Delta\varphi$ bins with $\Delta\eta = 0$.

In the analysis reported in this paper, a small relative rise in the correlation structure around $\Delta\varphi = \pi$ at large $\Delta\eta$ has been observed. This structure, which was already reported in previous studies [43, 55], is usually indicated as "wings". These wings are an artifact introduced by the mixed-event correlation, which does not match the shape of the background perfectly due to the finite binning in multiplicity and PV position along the beam axis. Hence, the correlation function is scaled once more with a 2D distribution constant in $\Delta\varphi$ and dependent on $\Delta\eta$ in order to get a flat distribution in $\Delta\eta$ in the away side.

In the case of V^0 trigger particles, the correlation function in Eq. 1 is obtained for K^0_S and Λ candidates reconstructed in the invariant mass ranges $|m_{V^0} - M| < 3\sigma$, M being the corresponding mass of the particle as given by the PDG [45]. However, the angular correlation also contains contributions from combinatorial background candidates in this mass range, and this source of background needs to be subtracted. This contribution is estimated via the per-trigger correlation distribution built from background trigger candidates in the side-band invariant mass ranges $5\sigma < |m_{V^0} - M| < 8\sigma$.

For the measurement of I_{AA}, the yield of associated particles per trigger particle is studied as a function of the azimuthal angle difference $\Delta\varphi$ in pp and Pb–Pb collisions. This distribution is given by

$$C(\Delta\varphi) = \frac{1}{N_{\text{trig}}} \frac{\mathrm{d}N_{\text{assoc}}}{\mathrm{d}\Delta\varphi}. \tag{2}$$

This quantity is measured for all pairs of particles where $p_{\text{T,assoc}} < p_{\text{T,trig}}$ within $|\Delta\eta| < 0.7$ as a function of $p_{\text{T,assoc}}$. Since the anisotropic flow induces a $\Delta\varphi$ dependent modulation of the background that cannot be neglected in Pb–Pb collisions, the background contributions to the yield extraction in Pb–Pb are modelled as

$$B(\Delta\varphi) = B_0 \left(1 + 2\sum_n v_n^{\text{trig}} v_n^{\text{assoc}} \cos(n\Delta\varphi)\right), \tag{3}$$

where v_n^{trig} and v_n^{assoc} are the flow coefficients for trigger and associated particles, respectively. Note that in this analysis only values of $n = 2, 3$ are considered. The data of v_n^{assoc} for charged particles and v_n^{trig} for V^0 particles are taken from Ref. [56].

The constant B_0 is determined with the zero yield at minimum (ZYAM) method, i.e., it is defined as the average value of six bins in the $C(\Delta\varphi)$ distributions outside of the jet peaks where the background is assumed to be flat [27, 44, 50, 57]. The ZYAM method is also used to subtract the pedestal in pp collisions. Finally, the jet-like correlations are obtained as

$$J(\Delta\varphi) = C(\Delta\varphi) - B(\Delta\varphi). \tag{4}$$

To access the nuclear modification factor, I_{AA}, the ratio of the integrated jet-like charged hadron yield in Pb–Pb collisions over that in pp collisions is calculated according to the following equation:

$$I_{AA} = \int_X J_{Pb-Pb}(\Delta\varphi)\mathrm{d}\Delta\varphi \Big/ \int_X J_{pp}(\Delta\varphi)\mathrm{d}\Delta\varphi, \tag{5}$$

where J_{Pb-Pb} and J_{pp} are the jet-like charged hadron yields in Pb–Pb and pp collisions, respectively, and X denotes either the near-side $|\Delta\varphi| < 0.9$ or the away-side $|\Delta\varphi - \pi| < 1.2$ region. The I_{AA} is measured for the near and away sides in 0–10% central Pb–Pb collisions at $\sqrt{s_{NN}}$ = 5.02 TeV, for unidentified charged hadrons with transverse momentum $1 < p_{T,assoc} < 8$ GeV/c associated with K_S^0, $\Lambda/\overline{\Lambda}$, and charged hadron triggers with transverse momentum $8 < p_{T,trig} < 16$ GeV/c.

3.3 Systematic uncertainty estimation

The sources of systematic uncertainties for the per-trigger yield and I_{AA} measurements on both the near and away sides in Pb–Pb and pp collisions are listed in Tables 2 and 3 for K_S^0–h and $(\Lambda+\overline{\Lambda})$–h angular correlations, respectively and in Table 4 for h–h correlations. Since the uncertainties are $p_{T,assoc}$ dependent, the minimum and maximum values of the contribution of each source are shown. The following main sources of systematic uncertainty are considered: systematic effect originating from the detector acceptance and, in particular, from the selection on the primary vertex position along the beam axis, systematic related to the track and V^0 reconstruction and selection, systematic uncertainty induced by the applied corrections (background invariant mass range, binning and scaling of the event-mixing correlations, wing correlation shape at large $\Delta\eta$, pedestal determination) and by the $\Delta\varphi$ integration window.

For the uncertainty related to the detector acceptance, the primary vertex position selection along the beam axis is decreased from ±10 cm to ±8 cm from the nominal interaction point position in the case of pp collisions and from ±7 cm to ±5 cm in the case of Pb–Pb collisions.

Systematic uncertainties related to the V^0 reconstruction are estimated by varying the topological selection criteria around their nominal values listed in Table 1. Two different sets of criteria (tight and loose) are used, which have a different magnitude and p_T dependence of the efficiency, thus impacting on the p_T distribution of selected V^0 trigger particles and on their correlation shapes.

The uncertainty from track selection is estimated by varying the track selection criteria between hybrid tracks and global tracks discussed in Sec. 3.1. In the case of global tracks, a stricter transverse momentum dependent requirement in the value of the DCA in the transverse plane results in reducing even further the amount of secondary particles in the track sample.

In addition, the sideband invariant mass intervals used to estimate the combinatorial background under the V^0 signals (see Sec. 3.2) are varied within $\pm1\sigma$ in order to estimate the uncertainty related to the background subtraction procedure.

The event-mixing technique is used for the acceptance correction by combining tracks originating from events close in multiplicity and PV position. The vertex binning is then varied as well as the mixed-event

scaling factor. Both variations produce non-negligible contributions to the total systematic uncertainties especially for K_S^0 and Λ. For more details see Tables 2, 3, 4.

The wing effect at large $\Delta\eta$ which is only observed in Pb–Pb collisions is studied. The contribution to the systematic uncertainties is found to be small for the measurements of Λ–h and h–h correlations while it is negligible for K_S^0–h correlations.

The uncertainty from the pedestal determination is estimated by shifting the ZYAM determination from using the default six bins to four bins on the left and right side of the near-side peak in the $\Delta\varphi$ distribution, as well as by fitting the full $\Delta\varphi$ region between the near and away sides. The largest effect to the uncertainty on the per-trigger yields for Pb–Pb collisions arises from this source, especially at low p_T.

Finally, the integration window for the near and away side is varied around the nominal values $|\Delta\varphi| < 0.9$ and $|\Delta\varphi - \pi| < 1.2$ by ± 0.2 radians.

The systematic uncertainties on the per-trigger yields in pp and Pb–Pb collisions as well as on I_{AA} are computed for each source separately. Due to correlations, the systematic uncertainties from some of the sources (e.g. invariant mass range and track selection) cancel out partially in the I_{AA}. The resulting uncertainties depend on $p_{T,assoc}$ and only the minimum and maximum values are reported in Tables 2, 3, 4. Finally, the total uncertainties are computed for the yields and the I_{AA} by summing in quadrature the contributions of the different sources.

Table 2: Summary of the different sources and corresponding estimated systematic uncertainties for the per-trigger yield of K_S^0–h correlations on the near and away sides in pp and Pb–Pb (0–10%) collisions, as well as for the I_{AA}. The systematic uncertainties depend on $p_{T,assoc}$ and for each source the minimum and maximum values are reported.

Uncertainty source	Near side (K_S^0–h)			Away side (K_S^0–h)		
	$Y(\Delta\varphi)$ pp	$Y(\Delta\varphi)$ Pb–Pb	I_{AA}	$Y(\Delta\varphi)$ pp	$Y(\Delta\varphi)$ Pb–Pb	I_{AA}
Primary vertex z	0–1.5%	1–5%	1–8%	0–2.7%	1–6%	1–9%
V^0 topology selections	0–0.4%	1–2%	0–1.8%	0–0.1%	1–6%	1–2%
Track selection	0–1%	1–2%	1–4%	0–1%	2–4%	2–5%
Invariant mass range	0–2.8%	1–2%	1–2%	0–2.7%	2–3.5%	0–1%
Mixing binning	0–0.4%	0–2%	1–2%	0–1.7%	0–6%	2–8%
Mixing scale	0–1.5%	1–3.5%	1–6%	0–2.7%	1–6%	1–7%
Wings correction	–	–	–	–	–	–
Pedestal determination	0–0.4%	1–10%	1–9%	0–1%	0–8%	2–11%
Integration window	0–0.2%	1–3.6%	1–3%	0–1%	1–2%	1–7%
Total	0–3.7%	2.6–12.9%	2.6–14.7%	0–5.2%	3.4–15.5%	4–19.8%

Table 3: Summary of the different sources and corresponding estimated systematic uncertainties for the per-trigger yield of ($\Lambda+\overline{\Lambda}$)–h correlations on the near and away sides in pp and Pb–Pb (0–10%) collisions, as well as for the I_{AA}. The systematic uncertainties depend on $p_{T,assoc}$ and for each source the minimum and maximum values are reported.

	Near side ($\Lambda+\overline{\Lambda}$)–h			Away side ($\Lambda+\overline{\Lambda}$)–h		
Uncertainty source	$Y(\Delta\varphi)$ pp	$Y(\Delta\varphi)$ Pb–Pb	I_{AA}	$Y(\Delta\varphi)$ pp	$Y(\Delta\varphi)$ Pb–Pb	I_{AA}
Primary vertex z	0–1.5%	1–7%	4–10%	0–1.8%	2–7%	3–11%
V^0 topology selections	0–1.3%	1–3.5%	1–5%	0–1%	0–6%	0–3%
Track selection	0–2.2%	1–4.2%	0–4.2%	0–2.5%	1–4%	1–3%
Invariant mass range	0–2.5%	0–5%	0–3%	0–2.5%	1–5%	0–3%
Mixing binning	0–1.7%	1–5%	2–7%	0–1.8%	0–3.5%	2–5%
Mixing scale	0–2.8%	1–3 %	2–10%	0–1.7%	0–4%	2–11%
Wings correction	–	0–1.8%	0–1.8%	–	0–1.8%	0–1.8%
Pedestal determination	0–0.2%	3–11%	2–15%	0–0.4%	1–9%	2–7%
Integration window	0–0.4%	1–3.5%	1–4 %	0–1	1–5%	1–5%
Total	0–5.1%	3.8–16.6%	5.5–23.3%	0–4.9%	2.8–16.2%	4.8–19.3%

Table 4: Summary of the different sources and corresponding estimated systematic uncertainties for the per-trigger yield of h–h correlations on the near and away sides in pp and Pb–Pb (0–10%) collisions, as well as for the I_{AA}. The systematic uncertainties depend on $p_{T,assoc}$ and for each source the minimum and maximum values are reported.

	Near side (h–h)			Away side (h–h)		
Uncertainty source	$Y(\Delta\varphi)$ pp	$Y(\Delta\varphi)$ Pb–Pb	I_{AA}	$Y(\Delta\varphi)$ pp	$Y(\Delta\varphi)$ Pb–Pb	I_{AA}
Primary vertex z	0–0.2%	0–2%	1–2%	0–0.2%	1–3%	0–4%
Track selection	0–1.7%	0–1.5%	0–1%	0–1.1%	1–2%	0–3%
Mixing binning	0–0.2%	0–2%	0–2%	0–0.2%	0–5.3%	0–2%
Mixing scale	0–1.7%	0–1.5%	0.2–3.8%	0–1.8%	0–2%	0–4%
Wings correction	–	0–1.2%	0–1.2%	–	0–1.3%	0–1.3%
Pedestal determination	0–0.2%	0–5%	0–4%	0–0.2%	2–7.7%	2–9.5%
Integration window	0–0.2%	0–0.7%	0–2%	0–0.2%	0–1%	0–1%
Total	0–2.5%	0–6.3%	1–6.7%	0–2.2%	2.4–10.3%	1.4–11.7%

4 Results and discussion

4.1 Projection of the correlation function $C(\Delta\varphi)$

The distributions of $C(\Delta\varphi)$ for the three different trigger particles with transverse momentum within $8 < p_{T,trig} < 16$ GeV/c, and associated charged particles of $4 < p_{T,assoc} < 6$ GeV/c, are presented in Fig. 1 for pp and 0–10% central Pb–Pb collisions. A uniform background in the case of pp is assumed, while the additional contributions of the anisotropic flow coefficients v_2 and v_3 in the case of Pb–Pb are subtracted.

The comparisons of $C(\Delta\varphi)$ distributions show a less pronounced away-side peak in central Pb–Pb collisions compared to pp collisions for the three trigger particle species. The per-trigger yields, obtained by integrating the correlation functions in the ranges of $|\Delta\varphi| < 0.9$ on the near side and $|\Delta\varphi - \pi| < 1.2$ on the away side have been studied as a function of $p_{T,assoc}$.
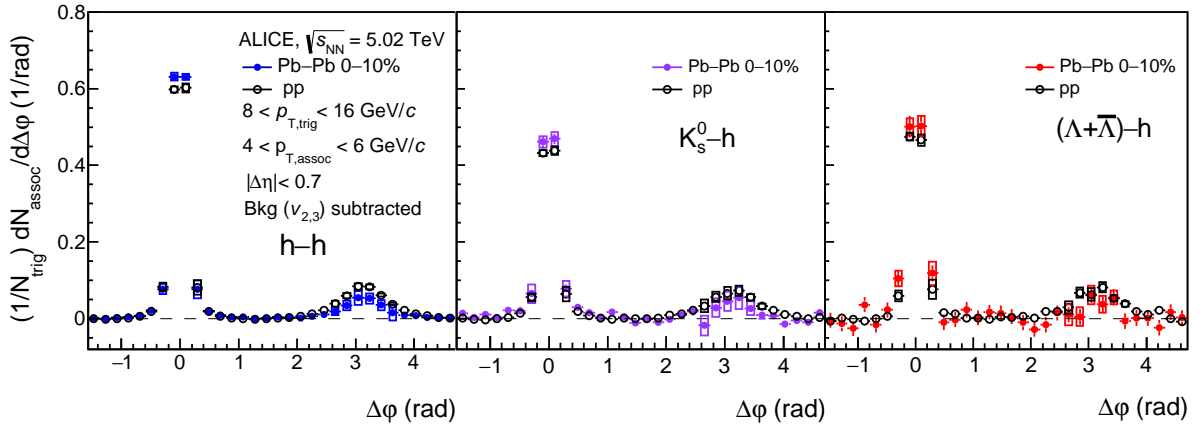
Figure 1: Distributions of $C(\Delta\varphi)$ for h–h (left), K_S^0–h (middle) and $(\Lambda+\overline{\Lambda})$–h (right) trigger particles with $8 < p_{T,trig} < 16$ GeV/c and associated particles with $4 < p_{T,assoc} < 6$ GeV/c in 0–10% central Pb–Pb (solid points) and pp (open circles) collisions. The error bars represent the statistical uncertainties while the boxes represent the systematic uncertainties. The background has been subtracted based on the estimation of ZYAM in pp collisions and the additional contributions of the anisotropic flow harmonics v_2 and v_3 in Pb–Pb collisions.

4.2   Nuclear modification factor I_{AA}

The ratio of the integrated peak yields for h–h, K_S^0–h, and $(\Lambda+\overline{\Lambda})$–h angular correlations in 0–10% central Pb–Pb collisions relative to pp collisions, I_{AA} defined in Eq. 5, is shown in the upper panels of Fig. 2 as a function of the associated particle p_T, $p_{T,assoc}$. In the away-side I_{AA} (top-right panel), a suppression of per-trigger yields in central Pb–Pb collisions to the level of $I_{AA} \approx 0.6$ for $p_{T,assoc} > 3$ GeV/c is observed for all trigger particles. This is expected to arise from the jet quenching effect on energetic partons caused by in-medium energy loss. However, going down in $p_{T,assoc}$, the I_{AA} ratio turns from suppression to enhancement reaching $I_{AA} \approx 2.7$. Such an enhancement could be expected based on energy conservation, with the high-p_T partons losing energy that gets converted into low-p_T associated particles. On the near side (top-left panel), a moderate enhancement of per-trigger yields in central Pb–Pb collisions for $p_{T,assoc} < 4$ GeV/c is observed, with I_{AA} reaching up to a value of about ≈ 1.8 for $1 < p_{T,assoc} < 3$ GeV/c. This enhancement suggests that the near-side parton is also subject to medium effects [26].

For associated particles with $p_{T,assoc} > 4$ GeV/c, the near-side I_{AA} results suggest a significantly smaller difference between pp and Pb–Pb collisions, which is consistent with trigger particles (having $p_{T,trig} > p_{T,assoc}$) predominantly coming from the hadronisation of partons produced on the surface of the medium and suffering minimal energy loss.

Within uncertainties, the measured I_{AA} shows no dependence on the trigger particle species for the considered $p_{T,trig}$ range, where measurements of the nuclear modification factor R_{AA} for different hadrons do not show any difference [24, 25, 58–60]. Such an observation provides additional insight into parton energy loss mechanisms in strongly interacting matter [34]. Thus, the I_{AA} results together with R_{AA} for identified hadrons can pose further constraints to theoretical models. The comparison of the I_{AA} measured from h–h correlations at $\sqrt{s_{NN}} = 5.02$ TeV with the results obtained via π^0–h and h–h correlations in Pb–Pb collisions at $\sqrt{s_{NN}} = 2.76$ TeV, published in [26, 27], is shown in the lower panels of Fig. 2. It illustrates a good agreement between the results at the two different collision energies.

The data are compared with theoretical models in Fig. 3, using the AMPT [61, 62] and HIJING [53] event generators. AMPT combines the initial particle distribution from HIJING with parton and hadron

cascades with elastic scatterings for final-state interactions. String melting with a parton interaction cross section of 1.5 mb and parton recombination for hadronisation are used with parameters from [61].

On the away side (right-hand panel), the AMPT calculation reproduces the data within uncertainties except for the enhancement at the lowest $p_{T,assoc}$, which is underestimated by the model. On the near side, it qualitatively describes the enhancement for the two lowest $p_{T,assoc}$ intervals but underestimates the measurements at high $p_{T,assoc}$, where the predicted suppression is clearly not observed in the data. The disagreement in this region may be related to the fact that AMPT was found to overpredict the single-particle R_{AA} at the LHC energies compared to RHIC energies [63]. The HIJING calculation, which includes the nuclear effects of jet quenching and parton shadowing, shows no modification on the near side but a suppression on the away side almost independent of $p_{T,assoc}$, which is different from the measured trend.
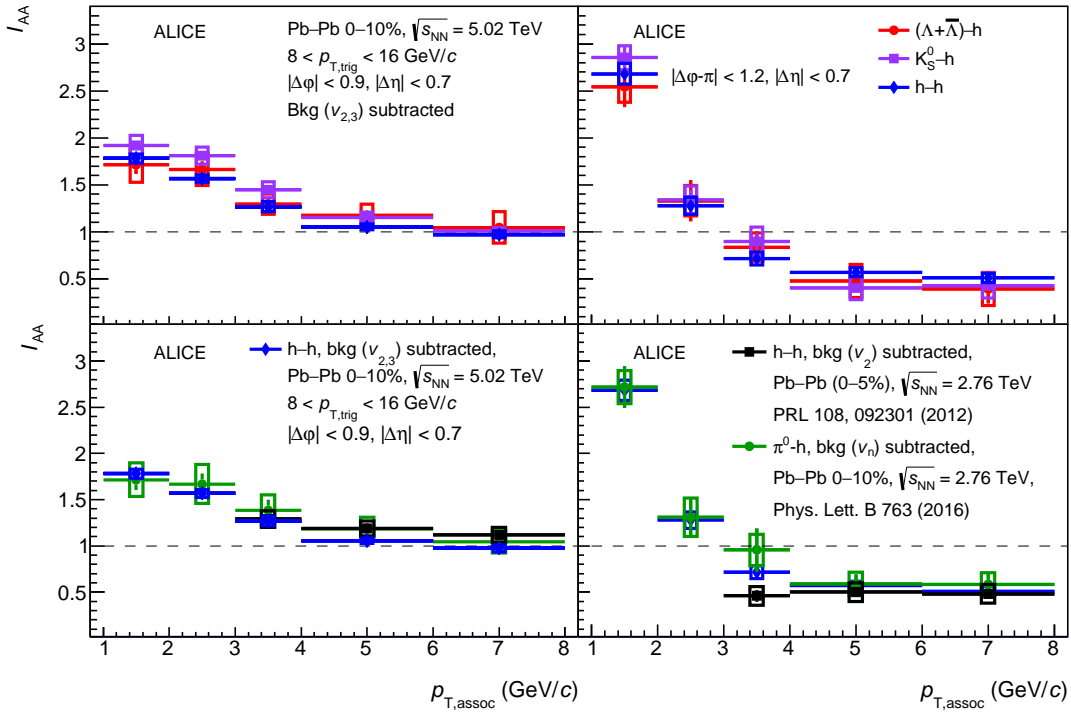

Figure 2: Top panel: per-trigger yield modification, I_{AA}, of K_S^0–h (square points), $(\Lambda+\overline{\Lambda})$–h (circle points) and h–h (diamond points), on the near side (left) and away side (right). Bottom panel: comparison of I_{AA} of h–h (diamond points) from this measurements at $\sqrt{s_{NN}}$ = 5.02 TeV, with I_{AA} of h–h (square points) and π^0–h (circle points) at $\sqrt{s_{NN}}$ = 2.76 TeV, on the near side (left) and away side (right) [26, 27].
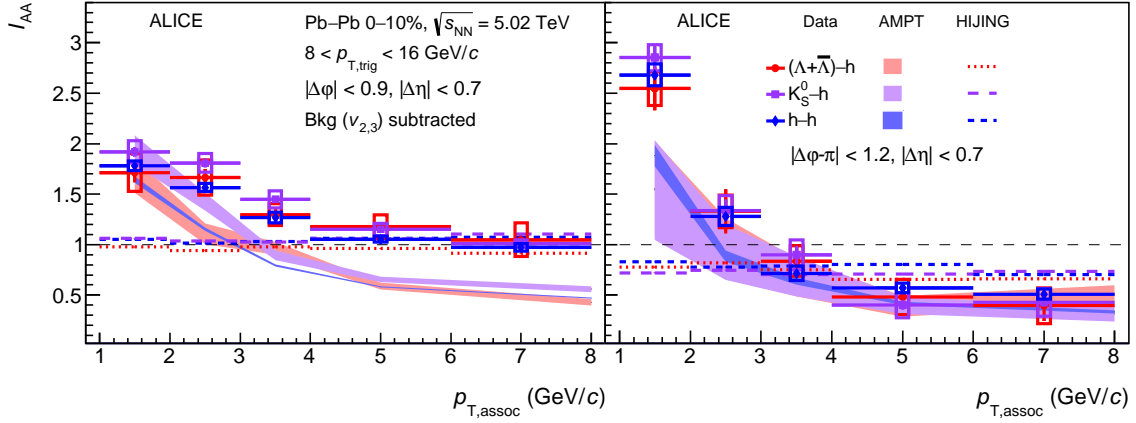
Figure 3: Per-trigger yield modification, I_{AA}, of K_S^0–h (square points), $(\Lambda+\overline{\Lambda})$–h (circle points) and h–h (diamond points), on the near side (left) and away side (right), compared to model calculations from AMPT [61, 62] and HIJING [53] event generators.

4.3 V^0- to hadron-triggered yield ratios

To investigate the differences between the V^0-triggered and the unidentified h–h (a sample dominated by pions) yields, their ratios were calculated. In particular, the contribution of gluon jets may be different for K_S^0 and Λ at high p_T, with baryons dominantly produced from gluon jets [34]. These ratios as a function of $p_{T,assoc}$ for both pp and central Pb–Pb collisions are shown in Fig. 4. The results indicate that at low $p_{T,assoc}$ (< 4 GeV/c) on both the near and away sides, the differences between charged-hadron triggered yields and either K_S^0 or $(\Lambda+\overline{\Lambda})$ triggered yields are small, and their ratios are compatible with unity at $1 < p_{T,assoc} < 2$ GeV/c. On the near side (left panels), their ratio goes below unity for $p_{T,assoc} \gtrsim$ 3 GeV/c and it decreases with increasing $p_{T,assoc}$, approaching 0.7 in the highest $p_{T,assoc}$ interval of the measurement in both pp and Pb–Pb collisions. This may indicate a smaller amount of higher p_T particles in the jets triggered with a V^0 particle than in the jets triggered with an unidentified charged hadron. On the away side (right panels), the differences between V^0 and charged hadrons stay small and their ratio is consistent with unity within uncertainties in the whole $p_{T,assoc}$ region analysed. This indicates that the back-to-back jets fragment independently and thus the away-side jet fragmentation is not affected by the trigger particle species. Furthermore, a mild difference of the near-side yields at intermediate p_T is observed between K_S^0 and $(\Lambda+\overline{\Lambda})$ trigger particles in pp collisions. However, this mild difference is not visible in Pb–Pb collisions within uncertainties. No difference between trigger K_S^0 and $(\Lambda+\overline{\Lambda})$ is observed for the away-side yields for both collision systems.
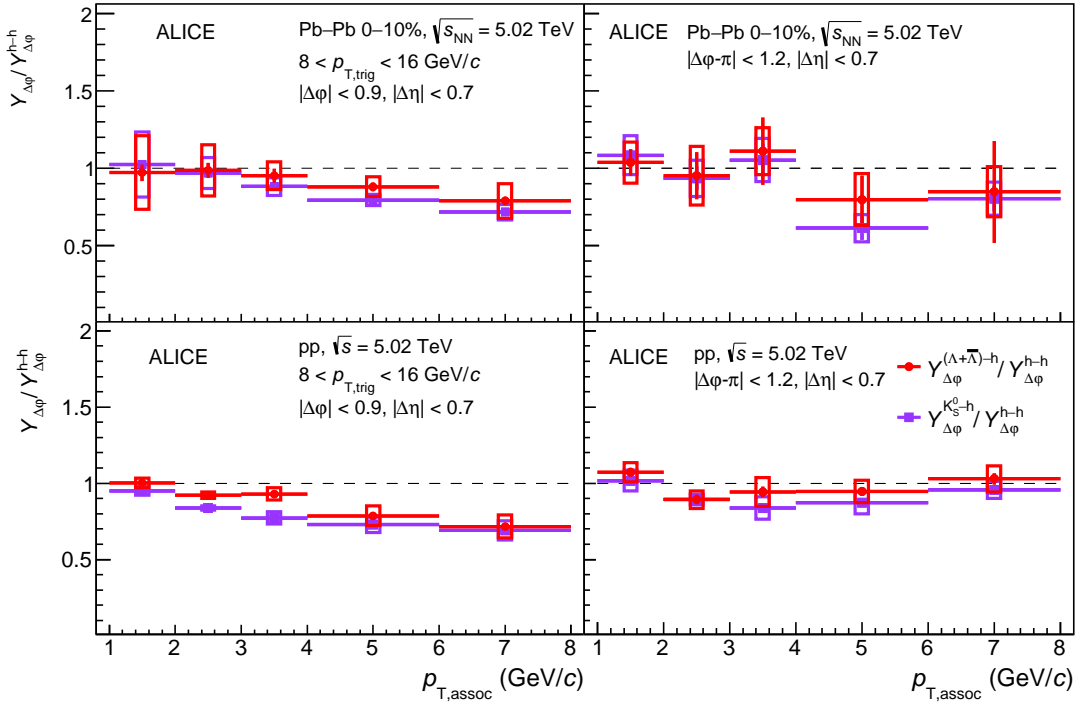
Figure 4: Ratios of V^0-triggered yields to charged-hadron triggered (h–h) ones, $Y_{\Delta\varphi}^{K_S^0-h}/Y_{\Delta\varphi}^{h-h}$ (square points) and $Y_{\Delta\varphi}^{(\Lambda+\bar{\Lambda})-h}/Y_{\Delta\varphi}^{h-h}$ (circle points), for Pb–Pb (top panels) and pp (bottom panels) collisions in near side (left) and away side (right).

5 Summary

Two-particle correlations have been measured as a function of the azimuthal angle difference $\Delta\varphi$ at midrapidity in pp and central Pb–Pb collisions at $\sqrt{s_{NN}} = 5.02$ TeV, with K_S^0, Λ, and charged hadrons of transverse momenta $8 < p_{T,trig} < 16$ GeV/c as trigger particles, and charged hadrons of transverse momenta $1 < p_{T,assoc} < 8$ GeV/c as associated particles.

The per-trigger yields for $|\Delta\varphi| < 0.9$ on the near side and $|\Delta\varphi - \pi| < 1.2$ on the away side have been extracted. The ratios of the per-trigger yields of associated charged hadrons in Pb–Pb collisions with respect to pp collisions, I_{AA}, have been calculated on the near and away sides. On the away side, the associated charged hadron yield in Pb–Pb collisions is suppressed relative to pp collisions, resulting in $I_{AA} \approx 0.6$ for $p_{T,assoc} > 3$ GeV/c, while an enhancement increasing with decreasing momentum is observed, resulting in $I_{AA} \approx 2.7$ at the lowest $p_{T,assoc}$. On the near side, an enhancement up to $I_{AA} \approx 1.8$ is observed at the lowest $p_{T,assoc}$. The coincidence of the enhancement at low p_T on the near and away side as well as the away-side suppression at high p_T suggests a common underlying mechanism, likely related to the energy lost by high-momentum partons, which is recovered in the surrounding medium as required by local energy conservation.

The I_{AA} of the yield associated with K_S^0 and ($\Lambda+\bar{\Lambda}$) triggers has been compared with the one measured with inclusive charged hadrons as trigger particles, as well as with results obtained from π^0−h and h–h correlations at $\sqrt{s_{NN}} = 2.76$ TeV. They are in good agreement within uncertainties on both the near and away sides, where the measurements of I_{AA} show no dependence on the trigger particle species. This measured trigger-hadron independence of I_{AA} between strange and non-strange particles and between

mesons and baryons provides new and important constraints for calculations of in-medium energy loss of high-p_T partons and their fragmentation properties, as well as the medium response to jets.

The measured I_{AA} is also compared to predictions from the AMPT and HIJING event generators: the AMPT calculation qualitatively describes the enhancement and suppression on the near and away sides, respectively. HIJING shows no modification on the near side and a suppression on the away side likely due to jet quenching but does not describe the p_T dependence observed in the measurements.

Moreover, the ratios of the per-trigger yields, $Y_{\Delta\varphi}^{(\Lambda+\overline{\Lambda})-h}/Y_{\Delta\varphi}^{h-h}$ and $Y_{\Delta\varphi}^{K_S^0-h}/Y_{\Delta\varphi}^{h-h}$, have been studied on the near and away sides in pp and central Pb–Pb collisions. A decreasing trend of the ratio with increasing $p_{T,assoc}$ is observed on the near side for both Pb–Pb and pp collisions, reaching values around 0.7 at the highest $p_{T,assoc}$. This may indicate a smaller amount of higher p_T particles in jets triggered with a V^0 particle than in jets triggered with an unidentified charged hadron. In addition, a mild difference between K_S^0 and Λ triggered correlations observed on the near side in pp collisions is not visible in Pb–Pb collisions within uncertainties. On the away side, the per-trigger yield ratio between V^0 and charged hadrons is consistent with unity within uncertainties in the whole $p_{T,assoc}$ region analysed, proving that the recoiling jet is independent from the trigger particle species.

References

[1] **BRAHMS** Collaboration, I. Arsene *et al.*, "Quark gluon plasma and color glass condensate at RHIC? The Perspective from the BRAHMS experiment", *Nucl. Phys. A* **757** (2005) 1–27, `arXiv:nucl-ex/0410020`.

[2] **PHOBOS** Collaboration, B. B. Back *et al.*, "The PHOBOS perspective on discoveries at RHIC", *Nucl. Phys. A* **757** (2005) 28–101, `arXiv:nucl-ex/0410022`.

[3] **STAR** Collaboration, J. Adams *et al.*, "Experimental and theoretical challenges in the search for the quark gluon plasma: The STAR Collaboration's critical assessment of the evidence from RHIC collisions", *Nucl. Phys. A* **757** (2005) 102–183, `arXiv:nucl-ex/0501009`.

[4] **PHENIX** Collaboration, K. Adcox *et al.*, "Formation of dense partonic matter in relativistic nucleus–nucleus collisions at RHIC: Experimental evaluation by the PHENIX collaboration", *Nucl. Phys. A* **757** (2005) 184–283, `arXiv:nucl-ex/0410003`.

[5] M. Gyulassy and X. N. Wang, "Multiple collisions and induced gluon Bremsstrahlung in QCD", *Nucl. Phys. B* **420** (1994) 583–614, `arXiv:nucl-th/9306003`.

[6] A. Majumder and M. van Leeuwen, "The Theory and Phenomenology of Perturbative QCD Based Jet Quenching", *Prog. Part. Nucl. Phys.* **66** (2011) 41–92, `arXiv:1002.2206 [hep-ph]`.

[7] **ALICE** Collaboration, K. Aamodt *et al.*, "Suppression of charged particle production at large transverse momentum in central Pb–Pb collisions at $\sqrt{s_{NN}} = 2.76$ TeV", *Phys. Lett. B* **696** (2011) 30–39, `arXiv:1012.1004 [nucl-ex]`.

[8] **PHENIX** Collaboration, K. Adcox *et al.*, "Suppression of hadrons with large transverse momentum in central Au+Au collisions at $\sqrt{s_{NN}} = 130$ GeV", *Phys. Rev. Lett.* **88** (2002) 022301, `arXiv:nucl-ex/0109003`.

[9] **STAR** Collaboration, L. Adamczyk *et al.*, "Jet-Hadron Correlations in $\sqrt{s_{NN}} = 200$ GeV $p+p$ and Central Au+Au Collisions", *Phys. Rev. Lett.* **112** (2014) 122301, `arXiv:1302.6184 [nucl-ex]`.

[10] **CMS** Collaboration, S. Chatrchyan *et al.*, "Observation and studies of jet quenching in Pb–Pb collisions at nucleon-nucleon center-of-mass energy $\sqrt{s_{NN}} = 2.76$ TeV", *Phys. Rev. C* **84** (2011) 024906, `arXiv:1102.1957 [nucl-ex]`.

[11] **ATLAS** Collaboration, G. Aad *et al.*, "Measurement of the jet radius and transverse momentum dependence of inclusive jet suppression in lead-lead collisions at $\sqrt{s_{NN}} = 2.76$ TeV with the ATLAS detector", *Phys. Lett. B* **719** (2013) 220–241, arXiv:1208.1967 [hep-ex].

[12] **ALICE** Collaboration, J. Adam *et al.*, "Measurement of jet suppression in central Pb–Pb collisions at $\sqrt{s_{NN}} = 2.76$ TeV", *Phys. Lett. B* **746** (2015) 1–14, arXiv:1502.01689 [nucl-ex].

[13] **ALICE** Collaboration, S. Acharya *et al.*, "Measurements of inclusive jet spectra in pp and central Pb–Pb collisions at $\sqrt{s_{NN}} = 5.02$ TeV", *Phys. Rev. C* **101** no. 3, (2020) 034911, arXiv:1909.09718 [nucl-ex].

[14] **ALICE** Collaboration, J. Adam *et al.*, "Measurement of jet quenching with semi-inclusive hadron-jet distributions in central Pb–Pb collisions at $\sqrt{s_{NN}} = 2.76$ TeV", *JHEP* **09** (2015) 170, arXiv:1506.03984 [nucl-ex].

[15] **ATLAS** Collaboration, G. Aad *et al.*, "Observation of a Centrality-Dependent Dijet Asymmetry in Lead-Lead Collisions at $\sqrt{s_{NN}} = 2.76$ TeV with the ATLAS Detector at the LHC", *Phys. Rev. Lett.* **105** (2010) 252303, arXiv:1011.6182 [hep-ex].

[16] **CMS** Collaboration, S. Chatrchyan *et al.*, "Jet momentum dependence of jet quenching in PbPb collisions at $\sqrt{s_{NN}} = 2.76$ TeV", *Phys. Lett. B* **712** (2012) 176–197, arXiv:1202.5022 [nucl-ex].

[17] **CMS** Collaboration, S. Chatrchyan *et al.*, "Studies of jet quenching using isolated-photon+jet correlations in Pb–Pb and pp collisions at $\sqrt{s_{NN}} = 2.76$ TeV", *Phys. Lett. B* **718** (2013) 773–794, arXiv:1205.0206 [nucl-ex].

[18] **ALICE** Collaboration, K. Aamodt *et al.*, "Suppression of charged particle production at large transverse momentum in central Pb–Pb collisions at $\sqrt{s_{NN}} = 2.76$ TeV", *Phys. Lett. B* **696** (2011) 30–39, arXiv:1012.1004 [nucl-ex].

[19] **CMS** Collaboration, S. Chatrchyan *et al.*, "Dependence on pseudorapidity and centrality of charged hadron production in Pb–Pb collisions at a nucleon-nucleon centre-of-mass energy of $\sqrt{s_{NN}} = 2.76$ TeV", *JHEP* **08** (2011) 141, arXiv:1107.4800 [nucl-ex].

[20] **CMS** Collaboration, S. Chatrchyan *et al.*, "Study of high-p_T charged particle suppression in Pb–Pb compared to pp collisions at $\sqrt{s_{NN}} = 2.76$ TeV", *Eur. Phys. J. C* **72** (2012) 1945, arXiv:1202.2554 [nucl-ex].

[21] **CMS** Collaboration, S. Chatrchyan *et al.*, "Measurement of jet fragmentation into charged particles in pp and Pb–Pb collisions at $\sqrt{s_{NN}} = 2.76$ TeV", *JHEP* **10** (2012) 087, arXiv:1205.5872 [nucl-ex].

[22] **ALICE** Collaboration, B. Abelev *et al.*, "Suppression of high transverse momentum D mesons in central Pb–Pb collisions at $\sqrt{s_{NN}} = 2.76$ TeV", *JHEP* **09** (2012) 112, arXiv:1203.2160 [nucl-ex].

[23] **ALICE** Collaboration, B. Abelev *et al.*, "Transverse momentum distribution and nuclear modification factor of charged particles in p–Pb collisions at $\sqrt{s_{NN}} = 5.02$ TeV", *Phys. Rev. Lett.* **110** no. 8, (2013) 082302, arXiv:1210.4520 [nucl-ex].

[24] **ALICE** Collaboration, B. B. Abelev *et al.*, "Production of charged pions, kaons and protons at large transverse momenta in pp and Pb–Pb collisions at $\sqrt{s_{NN}} =2.76$ TeV", *Phys. Lett. B* **736** (2014) 196–207, arXiv:1401.1250 [nucl-ex].

[25] **ALICE** Collaboration, J. Adam *et al.*, "Centrality dependence of the nuclear modification factor of charged pions, kaons, and protons in Pb–Pb collisions at $\sqrt{s_{NN}} = 2.76$ TeV", *Phys. Rev. C* **93** no. 3, (2016) 034913, `arXiv:1506.07287 [nucl-ex]`.

[26] **ALICE** Collaboration, K. Aamodt *et al.*, "Particle-yield modification in jet-like azimuthal di-hadron correlations in Pb–Pb collisions at $\sqrt{s_{NN}} = 2.76$ TeV", *Phys. Rev. Lett.* **108** (2012) 092301, `arXiv:1110.0121 [nucl-ex]`.

[27] **ALICE** Collaboration, J. Adam *et al.*, "Jet-like correlations with neutral pion triggers in pp and central Pb–Pb collisions $\sqrt{s_{NN}} = 2.76$ TeV", *Phys. Lett. B* **763** (2016) 238–250, `arXiv:1608.07201 [nucl-ex]`.

[28] **CMS** Collaboration, S. Chatrchyan *et al.*, "Very high-p_T triggered dihadron correlations in Pb–Pb and pp collisions at $\sqrt{s_{NN}} = 2.76$ TeV", *Nucl. Phys. A* **904–905** (2013) 451c–454c.

[29] **OPAL** Collaboration, G. Abbiendi *et al.*, "Particle multiplicity of unbiased gluon jets from e^+e^- three-jet events", *Eur. Phys. J. C* **23** (2002) 597–613, `arXiv:hep-ex/0111013`.

[30] **DELPHI** Collaboration, "Energy dependence of the differences between the quark and gluon jet fragmentation", *Z Phys C - Particles and Fields* **70** (1996) 179–195.

[31] E. Blanco, K. Kutak, W. Placzek, M. Rohrmoser, and K. Tywoniuk, "System of evolution equations for quark and gluon jet quenching with broadening", *Eur. Phys. J. C* **82** no. 4, (2022) 355, `arXiv:2109.05918 [hep-ph]`.

[32] **OPAL** Collaboration, K. Ackerstaff *et al.*, "Production of K$_S^0$ and Λ in quark and gluon jets from Z^0 decay", *Eur. Phys. J. C* **8** (1999) 241–254, `arXiv:hep-ex/9805025`.

[33] J.-W. Qiu, F. Ringer, N. Sato, and P. Zurita, "Factorization of jet cross sections in heavy-ion collisions", *Phys. Rev. Lett.* **122** no. 25, (2019) 252301, `arXiv:1903.01993 [hep-ph]`.

[34] W. Liu, C. M. Ko, and B. W. Zhang, "Jet conversions in a quark-gluon plasma", *Phys. Rev. C* **75** (2007) 051901, `arXiv:nucl-th/0607047`.

[35] **ALICE** Collaboration, B. B. Abelev *et al.*, "Multiplicity dependence of jet-like two-particle correlation structures in p–Pb collisions at $\sqrt{s_{NN}} = 5.02$ TeV", *Phys. Lett. B* **741** (2015) 38–50, `arXiv:1406.5463 [nucl-ex]`.

[36] **ALICE** Collaboration, J. Adam *et al.*, "Measurement of azimuthal correlations of D mesons and charged particles in pp collisions at $\sqrt{s} = 7$ TeV and p−Pb collisions at $\sqrt{s_{NN}} = 5.02$ TeV", *Eur. Phys. J. C* **77** no. 4, (2017) 245, `arXiv:1605.06963 [nucl-ex]`.

[37] **ALICE** Collaboration, S. Acharya *et al.*, "Jet fragmentation transverse momentum measurements from di-hadron correlations in $\sqrt{s} = 7$ TeV pp and $\sqrt{s_{NN}} = 5.02$ TeV p–Pb collisions", *JHEP.* **2019 03** no. 03, (2019) 169, `arXiv:1811.09742 [nucl-ex]`.

[38] **ALICE** Collaboration, S. Acharya *et al.*, "Jet-hadron correlations measured relative to the second order event plane in Pb–Pb collisions at $\sqrt{s_{NN}} = 2.76$ TeV", *Phys. Rev. C* **101** no. 6, (2020) 064901, `arXiv:1910.14398 [nucl-ex]`.

[39] I. Vitev, "Large angle hadron correlations from medium-induced gluon radiation", *Phys. Lett. B* **630** (2005) 78–84, `arXiv:hep-ph/0501255`.

[40] **ALICE** Collaboration, B. B. Abelev *et al.*, "Performance of the ALICE Experiment at the CERN LHC", *Int. J. Mod. Phys. A* **29** (2014) 1430044, `arXiv:1402.4476 [nucl-ex]`.

[41] **ALICE** Collaboration, K. Aamodt *et al.*, "The ALICE experiment at the CERN LHC", *Journal of Instrumentation* **3** (2008) S08002–S08002.

[42] **ALICE** Collaboration, B. B. Abelev *et al.*, "K$_S^0$ and Λ production in Pb–Pb collisions at $\sqrt{s_{NN}}$ = 2.76 TeV", *Phys. Rev. Lett.* **111** (2013) 222301, arXiv:1307.5530 [nucl-ex].

[43] **ALICE** Collaboration, S. Acharya *et al.*, "K$_S^0$- and (anti-)Λ-hadron correlations in pp collisions at $\sqrt{s}$ = 13 TeV", *Eur. Phys. J. C* **81** no. 10, (2021) 945, arXiv:2107.11209 [nucl-ex].

[44] **ALICE** Collaboration, S. Acharya *et al.*, "Anisotropic flow of identified particles in Pb–Pb collisions at $\sqrt{s_{NN}}$ = 5.02 TeV", *JHEP* **09** (2018) 006, arXiv:1805.04390 [nucl-ex].

[45] **Particle Data Group** Collaboration, P. A. Zyla *et al.*, "Review of particle physics", *Progress of Theoretical and Experimental Physics* **2020** (2020) 083C01.

[46] **ALICE** Collaboration, S. Acharya *et al.*, "Measurement of charged jet cross section in pp collisions at $\sqrt{s}$ = 5.02 TeV", *Phys. Rev. D* **100** no. 9, (2019) 092004, arXiv:1905.02536 [nucl-ex].

[47] **ALICE** Collaboration, S. Acharya *et al.*, "Constraining the Chiral Magnetic Effect with charge-dependent azimuthal correlations in Pb–Pb collisions at $\sqrt{s_{NN}}$ = 2.76 and 5.02 TeV", *JHEP* **09** (2020) 160, arXiv:2005.14640 [nucl-ex].

[48] J. Podolanski and R. Armenteros, "III. Analysis of V-events", *The London, Edinburgh, and Dublin Philosophical Magazine and Journal of Science* **45** no. 360, (1954) 13–30.

[49] P. B. Rodríguez *et al.*, "Calibration of the momentum scale of a particle physics detector using the Armenteros-Podolanski plot", *JINST* **16** no. 06, (2021) P06036, arXiv:2012.03620 [physics.ins-det].

[50] **ALICE** Collaboration, B. Abelev *et al.*, "Long-range angular correlations on the near and away side in p–Pb collisions at $\sqrt{s_{NN}}$ = 5.02 TeV", *Phys. Lett. B* **719** (2013) 29–41, arXiv:1212.2001 [nucl-ex].

[51] T. Sjostrand, S. Mrenna, and P. Z. Skands, "A Brief Introduction to PYTHIA 8.1", *Comput. Phys. Commun.* **178** (2008) 852–867, arXiv:0710.3820 [hep-ph].

[52] P. Skands, S. Carrazza, and J. Rojo, "Tuning PYTHIA 8.1: the Monash 2013 Tune", *Eur. Phys. J. C* **74 (8),** 3024 (2014), arXiv:1404.5630 [hep-ph].

[53] M. Gyulassy and X.-N. Wang, "HIJING 1.0: A Monte Carlo program for parton and particle production in high-energy hadronic and nuclear collisions", *Comput. Phys. Commun.* **83** (1994) 307, arXiv:nucl-th/9502021.

[54] R. Brun, F. Bruyant, F. Carminati, S. Giani, M. Maire, A. McPherson, G. Patrick, and L. Urban, *GEANT Detector Description and Simulation Tool, CERN-W-5013 , 1 (1994), https://doi.org/10.17181/CERN. MUHF.DMJ1.*

[55] **ALICE** Collaboration, J. Adam *et al.*, "Evolution of the longitudinal and azimuthal structure of the near-side jet peak in Pb–Pb collisions at $\sqrt{s_{NN}}$ = 2.76 TeV", *Phys. Rev. C* **96** no. 3, (2017) 034904, arXiv:1609.06667 [nucl-ex].

[56] **ALICE** Collaboration, S. Acharya *et al.*, "Anisotropic flow of identified particles in Pb-Pb collisions at $\sqrt{s_{NN}}$ = 5.02 TeV", *JHEP* **09** (2018) 006, arXiv:1805.04390 [nucl-ex].

[57] T. A. Trainor, "Zero yield at minimum (ZYAM) method and v_2: Underestimating jet yields from dihadron azimuth correlations", *Phys. Rev. C* **81** (2010) 014905, arXiv:0904.1733 [hep-ph].

[58] **STAR** Collaboration, B. I. Abelev *et al.*, "Identified baryon and meson distributions at large transverse momenta from Au+Au collisions at $\sqrt{s_{NN}} = 200$ GeV", *Phys. Rev. Lett.* **97** (2006) 152301, arXiv:nucl-ex/0606003.

[59] **STAR** Collaboration, G. Agakishiev *et al.*, "Identified hadron compositions in p+p and Au+Au collisions at high transverse momenta at $\sqrt{s_{NN}} = 200$ GeV", *Phys. Rev. Lett.* **108** (2012) 072302, arXiv:1110.0579 [nucl-ex].

[60] **ALICE** Collaboration, S. Acharya *et al.*, "Production of charged pions, kaons, and (anti-)protons in Pb–Pb and inelastic pp collisions at $\sqrt{s_{NN}} = 5.02$ TeV", *Phys. Rev. C* **101** no. 4, (2020) 044907, arXiv:1910.07678 [nucl-ex].

[61] J. Xu and C. M. Ko, "Pb–Pb collisions at $\sqrt{s_{NN}} = 2.76$ TeV in a multiphase transport model", *Phys. Rev. C* **83** (2011) 034904, arXiv:1101.2231 [nucl-th].

[62] Z.-W. Lin, C. M. Ko, B.-A. Li, B. Zhang, and S. Pal, "A Multi-phase transport model for relativistic heavy ion collisions", *Phys. Rev. C* **72** (2005) 064901, arXiv:nucl-th/0411110.

[63] S. Pal and M. Bleicher, "Suppression of high p_T hadrons in Pb–Pb collisions at LHC", *Phys. Lett. B* **709** (2012) 82–86, arXiv:1201.2546 [nucl-th].

A   Appendix

A.1 V^0 to hadron-triggered yield ratios-compared to results at $\sqrt{s} = 13$ TeV

The yield ratios on the near and away sides, $Y_{\Delta\varphi}^{K_S^0-h}/Y_{\Delta\varphi}^{h-h}$ and $Y_{\Delta\varphi}^{(\Lambda+\overline{\Lambda})-h}/Y_{\Delta\varphi}^{h-h}$, in pp collisions at $\sqrt{s} = 5.02$ TeV are compared in Fig. A.1 to the corresponding results from pp collisions at $\sqrt{s} = 13$ TeV [43] with slight differences in $p_{T,trig}$ intervals, $\Delta\eta$ and $\Delta\varphi$ ranges. The results show that the ratio do not depend on $\sqrt{s}$ and $p_{T,trig}$ intervals within uncertainties. This is consistent with the fragmentation function being weakly dependent on collision energy in the LHC domain.
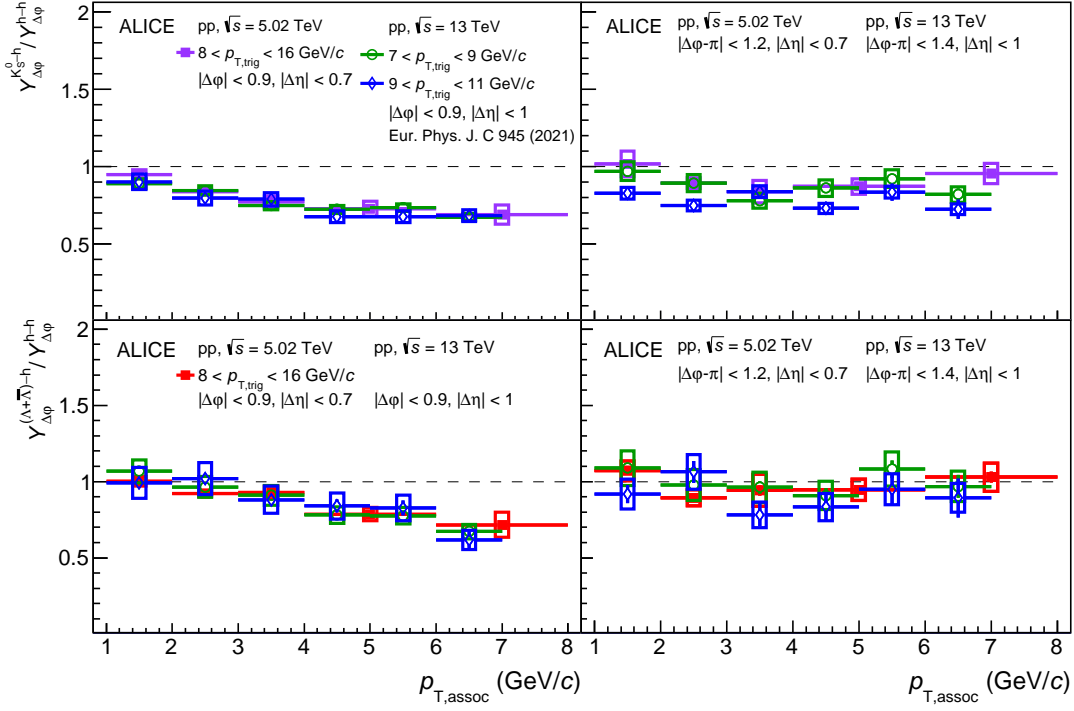

Figure A.1: Ratios of V^0-triggered yields to charged-hadron (h–h) yields, $Y_{\Delta\varphi}^{K_S^0-h}/Y_{\Delta\varphi}^{h-h}$ (top panels) and $Y_{\Delta\varphi}^{(\Lambda+\overline{\Lambda})-h}/Y_{\Delta\varphi}^{h-h}$ (bottom panels), for pp collisions on the near side (left) and away side (right) from this measurement compared with published results at higher collision energy [43].